Energy Storage Materials 73 (2024) 103808

Contents lists available at ScienceDirect

Energy Storage Materials

journal homepage: www.elsevier.com/locate/ensm

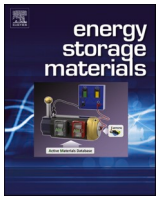

Identifying the importance of functionalization evolution during pre-oxidation treatment in producing economical asphalt-derived hard carbon for Na-ion batteries

Yuejing Zeng [a,1], Fei Wang [b,1], Yanbing Cheng [b], Minghui Chen [a], Jiyue Hou [b], Dong Yang [b], Yaqi Zhang [a], Wenhao Yang [b], Guanjun Liu [b], Yiyong Zhang [b], Ziyi Zhu [b], Xue Li [b,*], Yang Yang [a,*], Jinbao Zhao [a,*]

[a] State Key Lab of Physical Chemistry of Solid Surfaces, State-Province Joint Engineering Laboratory of Power Source Technology for New Energy Vehicle, College of Chemistry and Chemical Engineering, Xiamen University, Xiamen, 361005, China
[b] National and Local Joint Engineering Research Center of Lithium-ion Batteries and Materials Preparation Technology, Faculty of Metallurgical and Energy Engineering, Kunming University of Science and Technology, Kunming 650093, China

ARTICLE INFO

Keywords:
Hard carbon
Low-cost
Na-ion batteries
Structural evolution
Asphalt

ABSTRACT

Na-ion batteries (NIBs) are emerging as frontrunners for next-generation energy storage systems, boasting superior safety profiles and promising cost-effectiveness. A crucial hurdle in the commercialization of NIBs lies in developing cost-effective hard carbons (HC) with high carbon yields. This work leverages ultra-affordable asphalt as a precursor, coupled with pre-oxidization to specifically tailor the microstructures of HC, achieving an impressive carbon yield of 63%. Both experimental and theoretical calculation results reveal that the successful introduction of oxidation sites during the pre-oxidation process is a prerequisite for producing non-graphitizable HC with large interlayer spacing. The inclusion of carbonyl groups effectively restricts the movement of carbon atoms during subsequent carbonization, thus hindering the graphitization of carbon layer. Furthermore, abundant ether-oxygen bonds enable the solid-phase carbonization mechanism and prevent the shrinkage of carbon layers, facilitating the crispation of carbon layers. This breakthrough significantly boosts the potential of harnessing low-cost, high-performance HC for NIBs.

1. Introduction

Lithium-ion batteries (LIBs) have maintained a dominant role in major energy storage systems since their commercial debut. However, the resource scarcity and escalating costs of lithium resources have increased manufacturing expenses, presenting obstacles to further technological progress [1]. Na-ion batteries (NIBs) are emerging as a promising alternative due to their superior safety performance, cost-effectiveness, and low toxicity [2]. Experience in battery development highlights the importance of identifying low-cost, high--performance electrode materials for the commercial success of NIBs [3]. Graphite, traditionally used as an anode in LIBs, is limited in NIBs applications due to difficulties in forming stable intercalation compounds with Na^+ [4–6]. Therefore, there is a critical need to intensively research alternative anode materials. A wide range of materials have been explored for NIBs applications, including carbon-based materials [7–9], alloys [10,11], metal oxides [12,13], organic compounds [14–16] and MXenes [17,18]. Among these, hard carbon (HC) is particularly notable for its abundant availability, straightforward synthesis, and cost-effectiveness [19,20].

Nonetheless, HC encounters several challenges, including low carbon yield, low initial coulombic efficiency (ICE), and unsatisfactory rate performance, which significantly hinder its commercialization [21]. Currently, common precursors for synthesizing HC include biomass [22,23], resin [24], coal [21] and asphalt [25–27]. Although biomass-derived HC offers relatively high capacity, it suffers from issues such as low carbon yield, volatile raw material sources, and unpredictable chemical reactions during synthesis. Additionally, the cost of HC rises due to low carbon yield and expensive intermediate processing, resulting in a higher cost-to-performance ratio, which makes it

* Corresponding authors.
E-mail addresses: 438616074@qq.com (X. Li), yangyang419@xmu.edu.cn (Y. Yang), jbzhao@xmu.edu.cn (J. Zhao).
[1] These author contributed equally to this work.

https://doi.org/10.1016/j.ensm.2024.103808
Received 14 June 2024; Received in revised form 3 September 2024; Accepted 23 September 2024
Available online 28 September 2024

unsuitable for mass production (Fig. 1**h**). Similarly, resin-based HC exhibits favorable electrochemical performance and consistency but is hindered by expensive precursors and the challenges associated with scaling production. The prohibitive cost and limited yield of these precursors, compounded by their complex and costly production methods, present significant barriers to their practical application. Thus, there is an urgent need to identify appropriate precursors that are both cost-effective and efficient in yield, while also providing outstanding electrochemical performance to achieve a lower cost-to-performance ratio.

Asphalt, a cost-effective petrochemical by-product (300 $ ton^{-1}), emerges as precursor with high carbon yield and benefits from well-established technology, positioning it as a prime candidate for large-scale production [30]. In 2011, Adelhelm et al. [31]. initially synthesized bitumen-derived HC for NIBs with a discharge capacity of only 130 mAh g^{-1} and an ICE of 14%. This shortfall can be attributed to the pronounced π-π interactions among the aromatic rings rich in hydrogen found in asphalt during carbonization. These interactions trigger condensation reactions, culminating in uncontrolled fusion-state carbonization. Consequently, the resulting carbon layers stack parallelly, leading to diminished interlayer spacings [32,33]. Subsequently, Daher et al. [34]. and Hu et al. [25]. improved the electrochemical performance of asphalt-based HC via pre-oxidation process, which introduced oxygen-containing functional groups into the asphalt's molecular structure and facilitated cross-linking reactions among aromatic rings. The subsequent carbonization process produced HC with disordered turbostratic nanodomains and expanded interlayer spacing. Oxygen plays a pivotal role in amorphous carbon, adeptly fine-tuning carbon layer formation during carbonization and simultaneously enhancing sodium storage capacity [35–37]. While leveraging oxygen-containing functional groups to optimize asphalt-derived HC holds promise, the inherent chemical reaction mechanisms and structure-electrochemical performance relationships require further exploration.

This work seeks to clarify the intricate structural evolution in asphalt during pre-oxidation treatment and its impact on the formation of HC during the carbonization process. By doing so, it aims to underscore the distinctive benefits of the pre-oxidation method in crafting HC for NIBs.

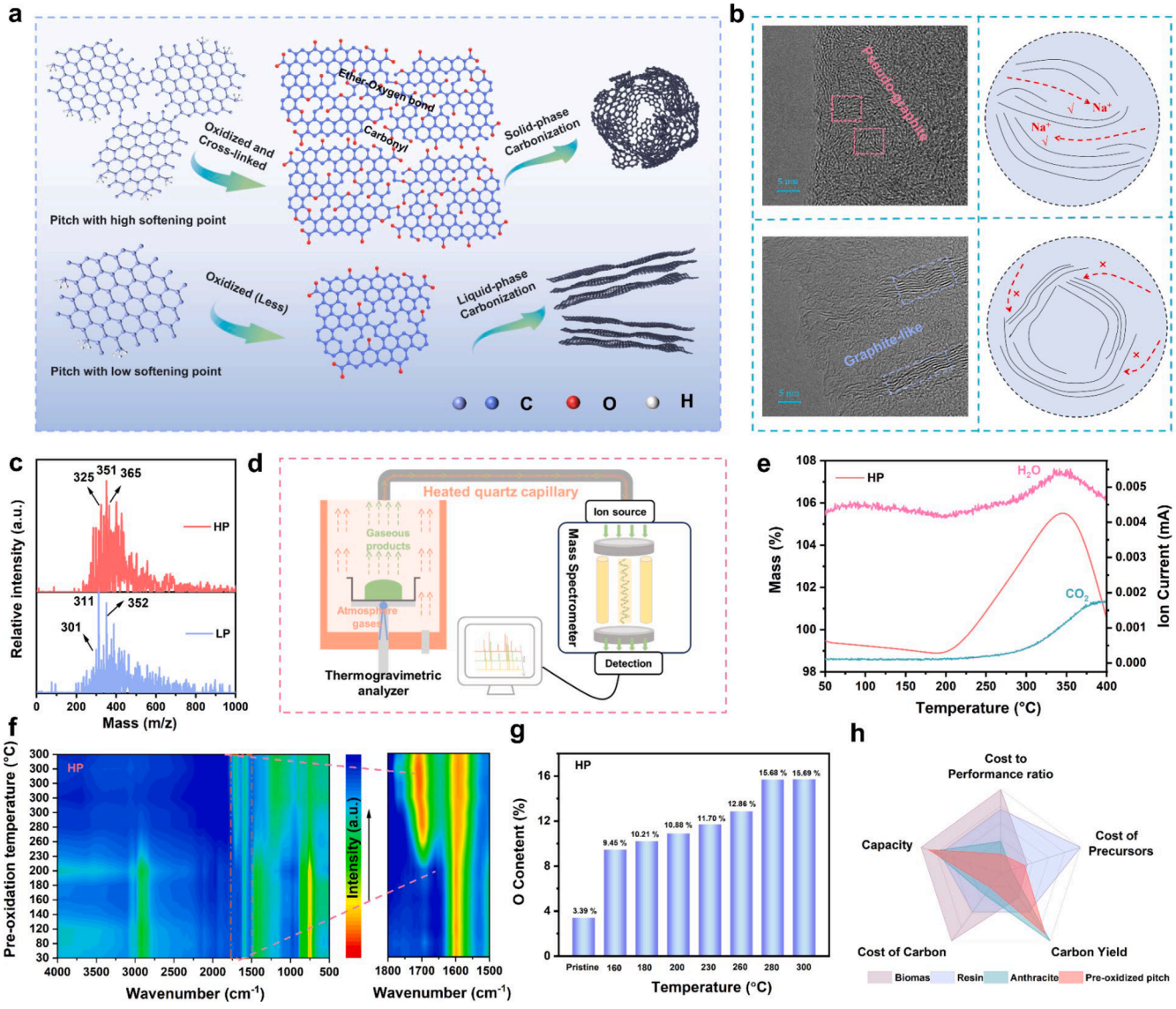

Fig. 1. a) Schematic illustration of pre-oxidization and carbonization process for pitches with different softening point. b) TEM images and the structural description for CHOP (upper) and CLOP (lower). c) MALDI-TOF/MS spectra for HP and LP. d) TG-MS schematic diagram for pitch. e) TG-MS result with the release of CO_2 (44 amu) and H_2O (18 amu) for HP. f) Ex-situ FT-IR spectra for HP during the pre-oxidization in air atmosphere at different temperatures. g) The O content of HP from XPS after pre-oxidization process. h) Radar plots of different precursors cross five key factors [21,25,28,29]..

However, asphalts with different softening points exhibit varying characteristics that significantly influence the structure and properties of the synthesized HC. Asphalts with higher softening points generally possess a more complex structure, characterized by a higher content of long-chain molecules and ring structures. This complexity provides increased structural stability and reduces sensitivity to high temperatures [38]. Therefore, two representative asphalts with high softening point (denoted as HP) and low softening point (denoted as LP) were utilized as precursors. Both HP and LP firstly experienced pre-oxidation treatment, resulting in oxidized asphalt (HOP and LOP) with subsequent carbonization process to obtain hard carbon denoted as CHOP and CLOP. As depicted in Fig. 1**a**, the pre-oxidation process adeptly integrates oxygen-containing functional groups into asphalt molecular, thereby effectively preventing asphalt melting during the subsequent carbonization process through the formation of a robust cross-linked network structure. Interestingly, minimal pre-oxidation occurs in LP, likely due to its comprising lower molecular weight components compared to HP. During the pre-oxidization process, the rate of formation of small volatile molecules from the asphalt surpasses that of oxidative cross-linking reactions. Hence, only asphalt of suitable molecular weight or high softening point can assure a proficient pre-oxidation process to yield asphalt-based HC characterized by an outstanding disordered microcrystalline structure. Through this investigation, we aspire to offer contemporary insights and methodologies for the efficient fabrication of HC for NIBs, thereby fostering its utilization and advancement in the realm of energy research.

2. Results and discussion

To comprehend the influence of pre-oxidation on the structure of HC, a series of measurements are conducted on CHOP and CLOP (**Fig. S2c**). TEM (Fig. 1**b)** indicates that CHOP is primarily composed of a turbine structure consisting of short-range ordered pseudo-graphite microdomains, while CLOP exhibits long-range ordered graphite microdomains. Such organized microdomain regions may hinder the rapid de-intercalation of Na^+. SEM (**Fig. S1**) shows that CHOP predominantly exhibits irregular particles, whereas CLOP displays flake-like structure with larger particle sizes. Furthermore, from X-ray diffraction (XRD) (**Fig. S2a**) CHOP displays classic broad peaks of (002) and (100) with larger interlayer spacing d_{002} (**Table S4**), while the (002) peak of CLOP appears as a relatively narrower peak, which is consistent with the Raman results (**Fig. S2b**). According to the fitting results (**Fig. S4**), CHOP exhibits a higher I_D/I_G ratio (1.3) compared to CLOP, indicating more disordered structure, which is more favorable for sodium storage. The distinct microcrystalline structures likely originate from variations in molecular structures and physical properties of asphalt precursors. Fig. 1**c** indicates that the overall molecular weight of HP is significantly higher than that of LP, which also results in a much higher softening point for HP (269 °C) compared to LP (193 °C) in **Table S1**. There is also distinct compositional difference between HP and LP, where HP has a higher proportion of aromatic hydrocarbons (**Table S2**), aligning with its elevated C/H ratio. Furthermore, the empirical factor aromaticity f_a (**Table S3**) [38] value of HP obtained from XRD fitting (**Fig. S3**) is significantly greater than that of LP, further confirming a higher proportion of aromatic hydrocarbons in HP.

To further elucidate the alterations during the pre-oxidation process of HP and LP, thermogravimetric (TG) test is initially conducted in an air atmosphere (**Fig. S5**). HP shows significant mass gain around 200 °C, peaking at approximately 320 °C, while LP demonstrates minimal mass gain. Expanding on the FT-IR analysis (**Fig. S6**), it is evident that subsequent to pre-oxidation at 300 °C for 6 h, HOP exhibits a discernible augmentation in carbonyl groups C = O (1710 cm^{-1}) and ether oxygen bonds -CH_2—O- (1184 cm^{-1}) compared to the unprocessed asphalts and LOP counterparts [25,39]. Concurrently, the vanishing of methyl and methylene (around 2800 cm^{-1}) and benzene ring (750 cm^{-1}) in HOP serves as additional evidence corroborating that the predominant transformation within HP entails dehydrogenation, oxidation, and fragmentation of aliphatic chains. The XPS findings (**Figs. S7** and **S8**) offer additional confirmation regarding the incorporation of oxygen into HOP. In the presence of oxygen, the components in asphalt undergo oxidation reactions, forming compounds with oxygen-containing functional groups. Moreover, SEM (**Fig. S9**) reveals an enlargement in the particle size of HOP compared to HP, furnishing empirical support for the efficacy of the pre-oxidation process. Further substantiation of the pre-oxidation process is attained via in-situ TG-MS analysis, delineated in Fig. 1**d**. HP predominantly releases H_2O and CO_2 during the process of mass gaining, consistent with the gases evolving during the pre-oxidation process (Fig. 1**e)**. Conversely, LP shows marginal mass augmentation along with minor generation of H_2O and CO_2 (**Fig. S10**). Additionally, Ex-situ FT-IR analysis is performed on HP subjected to pre-oxidation at diverse temperatures (Fig. 1**f, Fig. S11**). It is noted that with escalating temperatures, the appearance of carbonyl and ether oxygen bonds occur around 200 °C. Concurrent XPS analysis (Fig. 1**g**) provides additional insight, indicating a gradual increase in oxygen content of HOP with rising temperature, ultimately stabilizing around 300 °C. These alignment with the TG findings (**Fig. S5**) validates the successful incorporation of oxygen. These findings imply that the lower molecular weight of LP predominantly initiates decomposition reactions during the heat treatment in air. Moreover, the considerable presence of asphaltene renders it molten, inhibiting its interaction with air and consequently impeding the pre-oxidation reaction.

Next, classic molecular dynamics (MD) simulation is employed to illustrate the pre-oxidation and carbonization processes of HP in molecular-level. The initial model comprises 6180 carbon and 4098 hydrogen atoms, exhibiting a C/H ratio (**Fig. S13a**) closely resembling the experimental results, with model in **Fig. S12**. The simulation process commences with pre-oxidation in air atmosphere, followed by carbonization under oxygen-free conditions, as depicted in Fig. 2**a**. Specific simulation details are provided in the **Supporting Information**. The oxidized asphalt (Fig. 2**b**) displays prominent carbonyl and ether oxygen bonds, affirming the successful execution of the pre-oxidation process. The visualization process is depicted in **Video S1-S2**, corroborating the earlier analysis. Meanwhile, the oxidized asphalt comprises 5950 carbon, 3140 hydrogen, and 549 oxygen atoms, with a mass increase of 6.5% compared to pristine asphalt. This closely mirrors the experimental mass increase of 9.5% (**Fig. S5**), thereby underscoring the reliability of the computational results. The carbonization process is elucidated in **Video S3,** showcasing simulated HC (Fig. 2**c**) primarily composed of pseudo-graphite microdomains with distortion, consistent with the TEM findings. Upon further magnification (Fig. 2**d**), it becomes evident that closed pore structures form between the curved pseudo-graphite microdomains, offering supplementary sites for sodium storage. During carbonization process, the quantity of hexagonal rings initially decreases and then increases, suggesting the fracture and subsequent reconstruction of carbon chains (**Fig. S13b**). Furthermore, the evolving trend of hybridized carbon is illustrated (Fig. 2**f**), where the proportions of sp^2 C/sp^3 C align with the XPS results. Concurrently, the quantity of sp^2 C steadily diminishes with the advancement of carbonization, consistent with the pronounced defect values of CHOP [40]. On the contrary, the sp^2 C/sp^3 C ratio of CLOP (**Fig. S14**) is significantly higher than that of CHOP, suggesting a reduced presence of defects, consistent with the fitting results of Raman.

Furthermore, a more in-depth analysis of the pore structure of CHOP and CLOP is conducted. Firstly, the small-angle X-ray scattering (SAXS) curve of CHOP exhibits a more pronounced shoulder structure compared to CLOP, indicating a higher abundance of intrinsic micropores (Fig. 2**g**) [41–43]. Further refinement of the SAXS curve reveals that, for comparable pore sizes, CHOP is significantly more prevalent than CLOP (**Fig. S15**). The BET test (Fig. 2**h**) also reveals that CHOP delivers a greater specific surface area than CLOP. Additionally, the differential pore size distribution curves and the cumulative pore volume (**Fig. S16**) offer further evidence of abundant micropores and mesopores in CHOP,

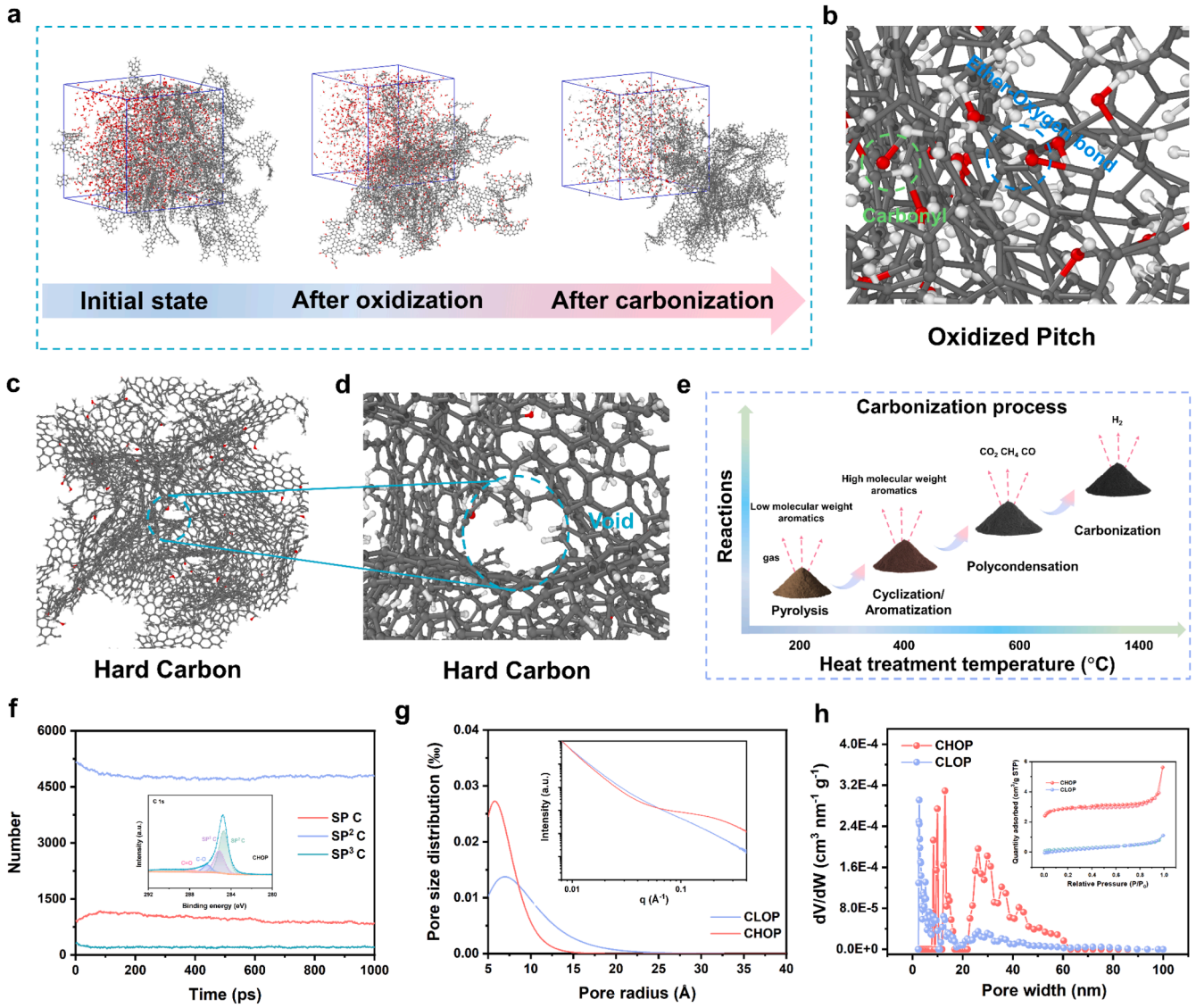

Fig. 2. a) MD model of asphalt structure at initial state, after oxidization and after carbonization. b) Asphalt configuration after pre-oxidization. c-d) Hard carbon structure after annealing. e) Schematic diagram of carbonization process. f) Change of structural composition for sample during carbonization process (inset: the high-resolution C 1 s spectra for CHOP). g) Pore size distribution from SAXS curve fitting (inset: SAXS patterns for CHOP and CLOP). h) Pore size distribution of CHOP and CLOP from non-local density functional theory (NLDFT) (inset: N_2 adsorption-desorption isotherms).

contrasting with CLOP (**Table S5**). The distinct microcrystalline and pore structures between CHOP and CLOP stem from varied reactions during the pre-oxidation and carbonization stages. There is a notable contrast in morphology between CHOP and CLOP (**Fig. S17**). CLOP displays a flake-like structure characteristic of liquid-phase carbonization [30], while CHOP maintains its original state through solid-phase carbonization [25]. The details of solid-phase carbonization are depicted in Fig. 2**e,** where at the beginning of pyrolysis, low-molecular-weight aromatics are released as gas because some of C—C bonds in organic molecules are weaker than C—H bonds [44,45]. Followed by cyclization and aromatization, the residues release high-molecular-weight aromatics. As temperature rises, polycondensation of aromatic molecules occurs, predominantly yielding gases like CO_2, CO and CH_4. Ultimately, almost all foreign atoms, mainly hydrogen go out and the residual solids are HC [44,45]. The solid-phase carbonization of HOP originates from the binding of carbonyl groups to carbon atoms and the tethering of ether oxygen bonds to carbon layers. This consequently results in HC containing more defects, underscoring the crucial role of the pre-oxidation process in forming asphalt-based HC with ideal microcrystalline structures.

The electrochemical behavior and sodium storage mechanism of HC will be further investigated in depth. Both CHOP and CLOP display the typical sloping capacity above 0.1 V and plateau capacity below 0.1 V (**Fig. S18a-b**), corresponding to the weak peak in the high-voltage region and the sharp peak near 0.1 V in the cyclic voltammetry (CV) curves (**Fig. S19**). The differential capacity vs. potential (dQ/dV) curve (**Fig. S20**) also exhibits a pair of distinct oxidation–reduction peaks around 0.1 V. Nevertheless, CHOP exhibits a slower decline with voltage compared to the sharp and linear decrease of CLOP (**Fig. S18c**) in the end of discharge. In-situ EIS (**Fig. S21**) reveals that during the discharge process, CLOP delivers one inflection point corresponding to two kinds of sodium storage mechanism. In contrast, combining in-situ EIS with curves of dQ/dV and Na^+ diffusion coefficient (Fig. 4**c**), CHOP delivers another inflection point in the end of the discharge process, which may indicate three kind of sodium storage mechanism [41,46].

Subsequently, we proceed to conduct additional research on the sodium storage behavior. Clearly, the Raman spectra of HC exhibits two characteristic peaks, namely the D band (1345 cm^{-1}) and the G band (1590 cm^{-1}), corresponding to defects in carbon and the E_{2g} vibration mode along the hexagonal carbon layers, respectively [47,48]. The ratio

of D band to G band intensity (I_D/I_G) serves as a parameter to assess the degree of defect level in carbon materials. The analogous changes observed in CHOP and CLOP during the in-situ Raman tests entail a redshift in the position of G band as sodiation process advances into plateau region (Fig. 3**a-b**). This occurs as a result of electron transfer, which weakens and elongates the C—C bonds, signifying Na^+ intercalation within the plateau region [41,49]. As discharge continues, the D band of CHOP gradually widens or fades, suggesting Na^+ adsorption at carbon edges or infiltration into pores, dampening carbon's breathing vibration [47]. In contrast, more stable D band of CLOP implies that Na^+ likely primarily adsorbs at defect sites with minimal pore filling. Furthermore, the significant displacement in the G band position between CHOP (58 cm^{-1}) and CLOP (30 cm^{-1}) may be attributed to a larger number of Na^+ storage sites in CHOP (Fig. 3**e-f**). Further in-situ XRD analysis (Fig. 3**c-d**) reveals that during sodiation process, the (002) peak of CLOP shifts to lower angles, followed by a return to higher angles during de-sodiation. According to the Bragg equation [50], the d_{002} of CLOP initially expands and then contracts, demonstrating Na^+ insertion behavior. Conversely, the position of (002) for CHOP remained relatively unchanged (Fig. 3**g**) with peak intensity fluctuations, suggesting the presence of Na^+ insertion behavior [41,51,52].

The preceding analysis has systematically understood the structural evolution of HC during the discharge and charge processes. Additionally, according to galvanostatic intermittent titration (GITT) (Fig. 4**a, Fig. S22**), Na^+ diffusion coefficients for CHOP decreases initially and then increases during the discharge process. This indicates that CHOP exhibits three types of sodium storage behaviors, which can be summarized as "adsorption-intercalation-pore filling," as inferred from the preceding analysis [41]. However, there is no subsequent increase observed in CLOP after decreasing, indicating an "adsorption-intercalation" sodium storage behavior. Numerous tests have been adopted to further validate the pore-filling sodium storage behavior. The SAXS intensity of fully discharged CHOP is notably lower than that of the pristine one, which is attributed to the filling of Na^+ in the pores, resulting in a reduction of electron density within the pores (Fig. 4**b**). Curves of dQ/dV and Na^+ diffusion coefficient (Fig. 4**c**) reveals that pore filling primarily occurs around 0.05 V at the end of discharge. Additionally, based on the ex-situ XPS testing (Fig. 4**d-e**), it is evident that as the discharge progresses, the Na 1 s peak position of CHOP shifts towards higher energy, indicating the formation of quasi-metallic sodium [53, 54]. On the contrary, the Na 1 s spectrum of CLOP shows almost no peak position shift. Furthermore, EPR testing (Fig. 4**g-h**) reveals that, compared to CLOP, fully discharged CHOP exhibits broader peak shapes, indicating the coexistence of Na^+ and quasi-metallic sodium [55–57]. The phenolphthalein coloration experiment (Fig. 4**j**) offers direct evidence of quasi-metallic sodium presence. When fully discharged CHOP and CLOP electrodes are desperately immersed in ethanol solutions with 1% phenolphthalein, CHOP turns purple with quasi-metallic sodium clusters, while CLOP remains unchanged [46,47]. The product was further identified as sodium ethoxide via ^1H NMR spectroscopy (**Fig. S23a**). The amount of quasi-metallic sodium stored in the CHOP was estimated using gas chromatography (GC) test, which measured the H_2 released from the reaction of quasi-metallic sodium with ethanol. Based on the released H_2 of 8720 ppm (**Fig. S23b**), the

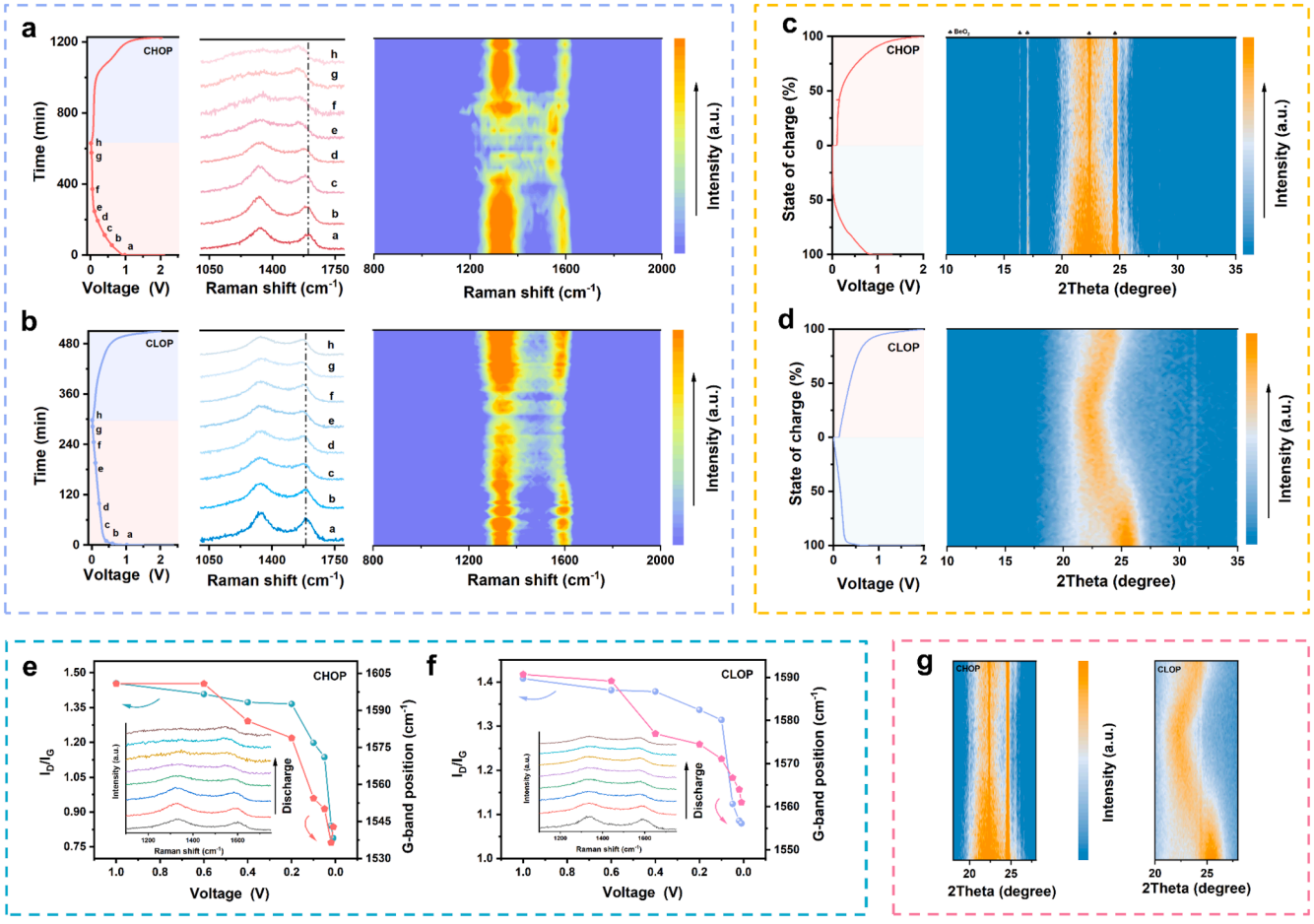

Fig. 3. In-situ Raman measurement for CHOP a) and CLOP b) during the first discharge-charge process. Operando XRD patterns in the initial cycling for CHOP c) and CLOP d). The value of I_D/I_G and the position of G-band vary with the voltage for CHOP e) and CLOP f) (inset: the corresponding magnified Raman spectra). g) Enlarged in-situ XRD contour maps of CHOP and CLOP.

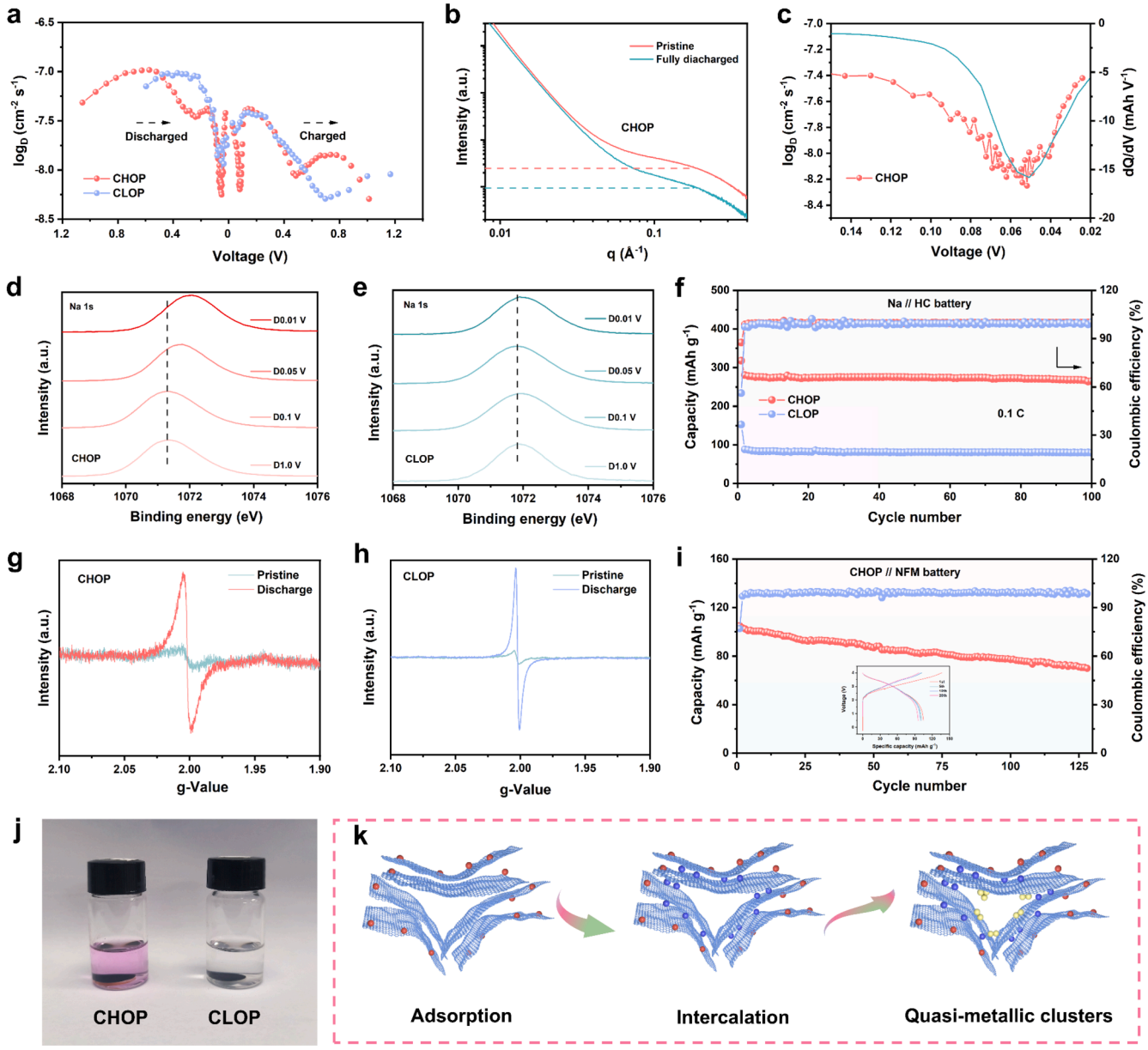

Fig. 4. a) The calculated Na^+ diffusion coefficient during the sodiation and de-sodiation process. b) SAXS profiles of CHOP at pristine and fully discharged state. c) dQ/dV curve from 0.15 to 0.02 V with corresponding diffusivity values for CHOP. Na 1 s spectra during various discharged state for CHOP d) and CLOP e). f) Cycling performance of half-cell Na // HC. The EPR spectra at pristine and fully discharged state for CHOP (g) and CLOP h). i) Cycling performance of full cell CHOP // NFM at 0.1 C (inset: corresponding charge/discharge curves at different cycles). j) Optical photograph of HC electrodes at fully sodiation state soaked in ethanol solution with 1% phenolphthalein. k) Proposed sodium storage mechanism.

rough content of quasi-metallic sodium in CHOP is calculated to be 1.24 $\times$ 10^{-5} mol g_{CHOP}^{-1} [20]. Upon comprehensive analysis, it's evident that CHOP primarily demonstrates "adsorption-intercalation-pore filling" sodium storage behavior (Fig. 4**k**). In contrast, due to the absence of closed pores, CLOP only undergoes "adsorption-intercalation" sodium storage behavior.

Finally, electrochemical performance tests are conducted. CHOP demonstrates notably higher reversible and plateau capacities compared to CLOP (**Fig. S24**), attributed to its more favorable microcrystalline structure and well-suited closed pore configuration. Figs. 4**f** and **Fig. S25** illustrate the cycling stability of CHOP and CLOP even at 1 C, highlighting high ICE (87.5%) and excellent cycling stability of CHOP, along with superior rate performance even at higher current density of 6 C in **Fig. S26**. Furthermore, full-cell CHOP // ($NaNi_{1/3}Fe_{1/3}Mn_{1/3}O_2$) NFM is also assembled (with an N/P ratio of 1.16), which delivers a discharge capacity of 104.9 mAh g^{-1} based on the mass of cathode electrode (Fig. 4**i**). In conclusion, CHOP demonstrates overall excellent electrochemical performance. Additionally, higher pre-oxidization temperature of 380 °C and 400 °C were employed to evaluate the electrochemical performance of the resulting hard carbons (CHOP-380 and CHOP-400). CHOP-380 and CHOP-400 exhibited only slight improvements over CHOP, likely due to the structural limitations of the asphalt, where minor increases in oxygen content are insufficient to overcome these constraints (**Fig. S27**). An asphalt with an intermediate softening point (MP) was used to further examine the effects of the pre-oxidation process (MOP) and the properties of the corresponding hard carbon (CMOP). Similar to HP, MP demonstrates mass gaining during pre-oxidation process, confirming successful oxidation. Correspondingly, CMOP displays stable cycling performance in half-cell Na//HC (**Fig. S28**). These findings suggest that only asphalts with appropriate

softening points can effectively introduce oxygen-containing groups and achieve superior electrochemical performance. To address the limitations of LP, mixtures of LP with various ratios of HP were tested. Electrochemical performance testing indicated that the mixtures offered slight improvements over CLOP (**Fig. S29**). However, the performance remained inferior to that of CHOP, indicating that mixing LP with HP reduces some of the drawbacks but fails to completely eliminate them.

3. Conclusion

In conclusion, asphalts with varying softening points are selected for research, revealing the correlation between asphalt structure and the pre-oxidation process, and providing a visualized analysis. Combining ex-situ FT-IR analysis with theoretical calculations, we elucidate that pre-oxidation only occurs in asphalt with higher softening points. The primary reactions involve dehydrogenation, oxidation, and cleavage of aliphatic chains, leading to the incorporation of carbonyl groups and ether oxygen bonds. The introduction of carbonyl groups effectively limits the activity of carbon atoms in subsequent carbonization processes, while ether oxygen bonds prevent the shrinkage of carbon layers. Both mechanisms contribute to the formation of microdomains in HC. In low softening point asphalt, the pre-oxidation process fails due to the decomposition rate surpassing the rate of reaction with air. Finally, owing to the successful pre-oxidation and cross-linking process, the resulting CHOP exhibits an enlarged d_{002} and increased closed pore volume, leading to enhanced electrochemical performance characterized by "adsorption-intercalation-pore filling" sodium storage behavior. In summary, inexpensive asphalt is a favorable option for HC synthesis, yet attention to asphalt structure is crucial. Only asphalt with a suitable structure can undergo successful pre-oxidation process, yielding appropriate HC structure. This study offers insights into achieving cost-effective production of high-quality HC.

4. Experimental section

Experimental details are provided in Supporting Information.

CRediT authorship contribution statement

Yuejing Zeng: Writing – original draft, Software, Methodology, Investigation, Formal analysis, Data curation, Conceptualization. **Fei Wang:** Writing – original draft, Methodology, Investigation, Formal analysis, Data curation, Conceptualization. **Yanbing Cheng:** Writing – review & editing, Software, Data curation. **Minghui Chen:** Writing – review & editing, Data curation. **Jiyue Hou:** Methodology. **Dong Yang:** Writing – review & editing. **Yaqi Zhang:** Writing – review & editing. **Wenhao Yang:** Writing – review & editing. **Guanjun Liu:** Writing – review & editing. **Yiyong Zhang:** Writing – review & editing. **Ziyi Zhu:** Writing – review & editing. **Xue Li:** Writing – review & editing, Supervision, Project administration, Funding acquisition. **Yang Yang:** Writing – review & editing, Supervision, Project administration, Funding acquisition. **Jinbao Zhao:** Writing – review & editing, Supervision, Resources, Project administration, Funding acquisition.

Declaration of competing interest

The authors declare that they have no known competing financial interests or personal relationships that could have appeared to influence the work reported in this paper.

Data availability

Data will be made available on request.

Acknowledgments

This work is supported by National Natural Science Foundation of China (No. 22379125, 22109030, and 22021001), Fundamental Research Funds for the Central Universities (20720220073), Fujian Industrial Technology Development and Application Plan (2022I0002), Yunnan Natural Science Foundation Project (202202AG050003) and Yunnan Natural Science Foundation Project (202101AW070006).

Supplementary materials

Supplementary material associated with this article can be found, in the online version, at doi:10.1016/j.ensm.2024.103808.

References

[1] D. Chen, W. Zhang, K. Luo, Y. Song, Y. Zhong, Y. Liu, G. Wang, B. Zhong, Z. Wu, X. Guo, Hard carbon for sodium storage: mechanism and optimization strategies toward commercialization, Energy Environ. Sci. 14 (2021) 2244–2262, https://doi.org/10.1039/D0EE03916K.
[2] Q. Wang, C. Zhao, Y. Lu, Y. Li, Y. Zheng, Y. Qi, X. Rong, L. Jiang, X. Qi, Y. Shao, D. Pan, B. Li, Y. Hu, L. Chen, Advanced Nanostructured Anode Materials for Sodium-Ion Batteries, Small 13 (2017) 1701835, https://doi.org/10.1002/smll.201701835.
[3] J. Wang, L. Xi, C. Peng, X. Song, X. Wan, L. Sun, M. Liu, J. Liu, Recent Progress in Hard Carbon Anodes for Sodium-Ion Batteries, Adv. Eng. Mater. 26 (2024) 2302063, https://doi.org/10.1002/adem.202302063.
[4] H. Wang, C. Zhu, D. Chao, Q. Yan, H.J. Fan, Nonaqueous Hybrid Lithium-Ion and Sodium-Ion Capacitors, Adv. Mater. 29 (2017) 1702093, https://doi.org/10.1002/adma.201702093.
[5] D. Xu, D. Chao, H. Wang, Y. Gong, R. Wang, B. He, X. Hu, H.J. Fan, Flexible Quasi-Solid-State Sodium-Ion Capacitors Developed Using 2D Metal–Organic-Framework Array as Reactor, Adv. Energy Mater. 8 (2018) 1702769, https://doi.org/10.1002/aenm.201702769.
[6] Z. Zheng, S. Hu, W. Yin, J. Peng, R. Wang, J. Jin, B. He, Y. Gong, H. Wang, H.J. Fan, CO_2 -Etching Creates Abundant Closed Pores in Hard Carbon for High-Plateau-Capacity Sodium Storage, Adv. Energy Mater. 14 (2023) 2303064, https://doi.org/10.1002/aenm.202303064.
[7] N. Sun, J. Qiu, B. Xu, Understanding of Sodium Storage Mechanism in Hard Carbons: ongoing Development under Debate, Adv. Energy Mater. 12 (2022) 2200715, https://doi.org/10.1002/aenm.202200715.
[8] G. Wang, M. Yu, X. Feng, Carbon materials for ion-intercalation involved rechargeable battery technologies, Chem. Soc. Rev. 50 (2021) 2388–2443, https://doi.org/10.1039/D0CS00187B.
[9] L. Zhao, Z. Hu, W. Lai, Y. Tao, J. Peng, Z. Miao, Y. Wang, S. Chou, H. Liu, S. Dou, Hard Carbon Anodes: fundamental Understanding and Commercial Perspectives for Na-Ion Batteries beyond Li-Ion and K-Ion Counterparts, Adv. Energy Mater. 11 (2021) 2002704, https://doi.org/10.1002/aenm.202002704.
[10] M. Lao, Y. Zhang, W. Luo, Q. Yan, W. Sun, S.X. Dou, Alloy-Based Anode Materials toward Advanced Sodium-Ion Batteries, Adv. Mater. 29 (2017) 1700622, https://doi.org/10.1002/adma.201700622.
[11] L. Fang, N. Bahlawane, W. Sun, H. Pan, B.B. Xu, M. Yan, Y. Jiang, Conversion-Alloying Anode Materials for Sodium Ion Batteries, Small 17 (2021) 2101137, https://doi.org/10.1002/smll.202101137.
[12] L. Wang, Z. Wei, M. Mao, H. Wang, Y. Li, J. Ma, Metal oxide/graphene composite anode materials for sodium-ion batteries, Energy Storage Mater 16 (2019) 434–454, https://doi.org/10.1016/j.ensm.2018.06.027.
[13] H. Liu, M. Jia, Q. Zhu, B. Cao, R. Chen, Y. Wang, F. Wu, B. Xu, 3D-0D Graphene-Fe_3O_4 Quantum Dot Hybrids as High-Performance Anode Materials for Sodium-Ion Batteries, ACS Appl. Mater. Interfaces 8 (2016) 26878–26885, https://doi.org/10.1021/acsami.6b09496.
[14] H. Wang, X. Zhang, Organic Carbonyl Compounds for Sodium-Ion Batteries: recent Progress and Future Perspectives, Chem. Eur. J. 24 (2018) 18235–18245, https://doi.org/10.1002/chem.201802517.
[15] Q. Zhao, A. Whittaker, X. Zhao, Polymer Electrode Materials for Sodium-ion Batteries, Materials (Basel) 11 (2018) 2567, https://doi.org/10.3390/ma11122567.
[16] X.-X. He, X.-H. Liu, Z. Yang, H. Zhang, L. Li, G. Xu, Y. Qiao, S.-L. Chou, M. Wu, Research progress of flexible sodium-ion batteries derived from renewable polymer materials, Electrochem. Commun. 128 (2021) 107067, https://doi.org/10.1016/j.elecom.2021.107067.
[17] P. Ma, D. Fang, Y. Liu, Y. Shang, Y. Shi, H.Y. Yang, MXene-Based Materials for Electrochemical Sodium-Ion Storage, Adv. Sci. 8 (2021) 2003185, https://doi.org/10.1002/advs.202003185.
[18] X. Guo, J. Zhang, J. Song, W. Wu, H. Liu, G. Wang, MXene encapsulated titanium oxide nanospheres for ultra-stable and fast sodium storage, Energy Storage Mater 14 (2018) 306–313, https://doi.org/10.1016/j.ensm.2018.05.010.
[19] Y. Chu, J. Zhang, Y. Zhang, Q. Li, Y. Jia, X. Dong, J. Xiao, Y. Tao, Q.-H. Yang, Reconfiguring Hard Carbons with Emerging Sodium-Ion Batteries: a Perspective, Adv. Mater. 35 (2023) 2212186, https://doi.org/10.1002/adma.202212186.

[20] H. Fang, S. Gao, M. Ren, Y. Huang, F. Cheng, J. Chen, F. Li, Dual-Function Presodiation with Sodium Diphenyl Ketone towards Ultra-stable Hard Carbon Anodes for Sodium-Ion Batteries, Angew. Chem. Int. Ed. 62 (2023) e202214717, https://doi.org/10.1002/anie.202214717.
[21] Y. Li, Y.-S. Hu, X. Qi, X. Rong, H. Li, X. Huang, L. Chen, Advanced sodium-ion batteries using superior low cost pyrolyzed anthracite anode: towards practical applications, Energy Storage Mater 5 (2016) 191–197, https://doi.org/10.1016/j.ensm.2016.07.006.
[22] Y. Li, Y. Hu, M. Titirici, L. Chen, X. Huang, Hard Carbon Microtubes Made from Renewable Cotton as High-Performance Anode Material for Sodium-Ion Batteries, Adv. Energy Mater. 6 (2016) 1600659, https://doi.org/10.1002/aenm.201600659.
[23] K. Hong, L. Qie, R. Zeng, Z. Yi, W. Zhang, D. Wang, W. Yin, C. Wu, Q. Fan, W. Zhang, Y. Huang, Biomass derived hard carbon used as a high performance anode material for sodium ion batteries, J. Mater. Chem. A 2 (2014) 12733, https://doi.org/10.1039/C4TA02068E.
[24] Y. Li, Y.-S. Hu, H. Li, L. Chen, X. Huang, A superior low-cost amorphous carbon anode made from pitch and lignin for sodium-ion batteries, J. Mater. Chem. A 4 (2016) 96–104, https://doi.org/10.1039/C5TA08601A.
[25] Y. Lu, C. Zhao, X. Qi, Y. Qi, H. Li, X. Huang, L. Chen, Y.-S. Hu, Pre-Oxidation-Tuned Microstructures of Carbon Anodes Derived from Pitch for Enhancing Na Storage Performance, Adv. Energy Mater. 8 (2018) 1800108, https://doi.org/10.1002/aenm.201800108.
[26] H. Guo, Y. Li, C. Wang, L. He, C. Li, Y. Guo, Y. Zhou, Effect of the air oxidation stabilization of pitch on the microstructure and sodium storage of hard carbons, New Carbon Mater 36 (2021) 1073–1078, https://doi.org/10.1016/S1872-5805(21)60075-6.
[27] J. Wang, J.-L. Liu, Y.-G. Wang, C.-X. Wang, Y.-Y. Xia, Pitch modified hard carbons as negative materials for lithium-ion batteries, Electrochim. Acta 74 (2012) 1–7, https://doi.org/10.1016/j.electacta.2012.03.099.
[28] Y. Li, Y.-S. Hu, H. Li, L. Chen, X. Huang, A superior low-cost amorphous carbon anode made from pitch and lignin for sodium-ion batteries, J. Mater. Chem. A 4 (2016) 96–104, https://doi.org/10.1039/c5ta08601a.
[29] Y. Li, Y. Lu, Q. Meng, A.C.S. Jensen, Q. Zhang, Q. Zhang, Y. Tong, Y. Qi, L. Gu, M. Titirici, Y. Hu, Regulating Pore Structure of Hierarchical Porous Waste Cork-Derived Hard Carbon Anode for Enhanced Na Storage Performance, Adv. Energy Mater. 9 (2019) 1902852, https://doi.org/10.1002/aenm.201902852.
[30] X. Yin, Y. Zhao, X. Wang, X. Feng, Z. Lu, Y. Li, H. Long, J. Wang, J. Ning, J. Zhang, Modulating the Graphitic Domains of Hard Carbons Derived from Mixed Pitch and Resin to Achieve High Rate and Stable Sodium Storage, Small 18 (2022) 2105568, https://doi.org/10.1002/smll.202105568.
[31] S. Wenzel, T. Hara, J. Janek, P. Adelhelm, Room-temperature sodium-ion batteries: improving the rate capability of carbon anode materials by templating strategies, Energy Environ. Sci. 4 (2011) 3342, https://doi.org/10.1039/c1ee01744f.
[32] J. Choi, Y. Lee, Y. Chae, S.-S. Kim, T.-H. Kim, S. Lee, Unveiling the transformation of liquid crystalline domains into carbon crystallites during carbonization of mesophase pitch-derived fibers, Carbon N Y 199 (2022) 288–299, https://doi.org/10.1016/j.carbon.2022.08.033.
[33] S. Chen, S. Xie, C. Fan, J. Guo, X. Li, Microstructure and performance of carbonization products of component from soft coal pitch, J. Saudi Chem. Soc. 22 (2018) 316–321, https://doi.org/10.1016/j.jscs.2016.06.003.
[34] D. Wang, E. Mejía, POSS-Based Nitrogen-Doped Hierarchically Porous Carbon as Metal-Free Oxidation Catalyst, ChemistrySelect 2 (2017) 3381–3387, https://doi.org/10.1002/slct.201700627.
[35] W. Chen, C. Chen, X. Xiong, P. Hu, Z. Hao, Y. Huang, Coordination of Surface-Induced Reaction and Intercalation: toward a High-Performance Carbon Anode for Sodium-Ion Batteries, Adv. Sci. 4 (2017) 1600500, https://doi.org/10.1002/advs.201600500.
[36] W. Shao, F. Hu, T. Zhang, S. Liu, C. Song, N. Li, Z. Weng, J. Wang, X. Jian, Engineering Ultramicroporous Carbon with Abundant C=O as Extended "Slope-Dominated" Sodium Ion Battery Anodes, ACS Sustain. Chem. Eng. 9 (2021) 9727–9739, https://doi.org/10.1021/acssuschemeng.1c01885.
[37] C. Chen, Y. Huang, Y. Zhu, Z. Zhang, Z. Guang, Z. Meng, P. Liu, Nonignorable Influence of Oxygen in Hard Carbon for Sodium Ion Storage, ACS Sustain. Chem. Eng. 8 (2020) 1497–1506, https://doi.org/10.1021/acssuschemeng.9b05948.
[38] C. Ge, Z. Sun, H. Yang, D. Long, W. Qiao, L. Ling, Preparation and characterization of high softening point and homogeneous isotropic pitches produced from distilled ethylene tar by a novel bromination method, New Carbon Mater 33 (2018) 71–81, https://doi.org/10.1016/S1872-5805(18)60327-0.
[39] X. Tang, F. Xie, Y. Lu, Z. Chen, X. Li, H. Li, X. Huang, L. Chen, Y. Pan, Y.-S. Hu, Intrinsic effects of precursor functional groups on the Na storage performance in carbon anodes, Nano Res 16 (2023) 12579–12586, https://doi.org/10.1007/s12274-023-5643-9.
[40] Y. Zhen, Y. Chen, F. Li, Z. Guo, Z. Hong, M.-M. Titirici, Ultrafast synthesis of hard carbon anodes for sodium-ion batteries, Proc. Natl. Acad. Sci. U. S. A. 118 (2021) e2111119118, https://doi.org/10.1073/pnas.2111119118.
[41] Y. Zeng, J. Yang, H. Yang, Y. Yang, J. Zhao, Bridging Microstructure and Sodium-Ion Storage Mechanism in Hard Carbon for Sodium Ion Batteries, ACS Energy Lett 9 (2024) 1184–1191, https://doi.org/10.1021/acsenergylett.3c02751.
[42] L. Kitsu Iglesias, E.N. Antonio, T.D. Martinez, L. Zhang, Z. Zhuo, S.J. Weigand, J. Guo, M.F. Toney, Revealing the Sodium Storage Mechanisms in Hard Carbon Pores, Adv. Energy Mater. 13 (2023) 2302171, https://doi.org/10.1002/aenm.202302171.
[43] Y. Chen, F. Li, Z. Guo, Z. Song, Y. Lin, W. Lin, L. Zheng, Z. Huang, Z. Hong, M.-M. Titirici, Sustainable and scalable fabrication of high-performance hard carbon anode for Na-ion battery, J. Power Sources 557 (2023) 232534, https://doi.org/10.1016/j.jpowsour.2022.232534.
[44] C. Wu, Y. Yang, Y. Zhang, H. Xu, X. He, X. Wu, S. Chou, Hard carbon for sodium-ion batteries: progress, strategies and future perspective, Chem. Sci. 15 (2024) 6244–6268, https://doi.org/10.1039/D4SC00734D.
[45] N. LeGe, X.-X. He, Y.-X. Wang, Y. Lei, Y.-X. Yang, J.-T. Xu, M. Liu, X. Wu, W.-H. Lai, S.-L. Chou, Reappraisal of hard carbon anodes for practical lithium/sodium-ion batteries from the perspective of full-cell matters, Energy Environ. Sci. 16 (2023) 5688–5720, https://doi.org/10.1039/D3EE02202A.
[46] Z. Wang, X. Feng, Y. Bai, H. Yang, R. Dong, X. Wang, H. Xu, Q. Wang, H. Li, H. Gao, C. Wu, Probing the Energy Storage Mechanism of Quasi-Metallic Na in Hard Carbon for Sodium-Ion Batteries, Adv. Energy Mater. 11 (2021) 2003854, https://doi.org/10.1002/aenm.202003854.
[47] Z. Tang, R. Zhang, H. Wang, S. Zhou, Z. Pan, Y. Huang, D. Sun, Y. Tang, X. Ji, K. Amine, M. Shao, Revealing the closed pore formation of waste wood-derived hard carbon for advanced sodium-ion battery, Nat. Commun. 14 (2023) 6024, https://doi.org/10.1038/s41467-023-39637-5.
[48] S. Komaba, W. Murata, T. Ishikawa, N. Yabuuchi, T. Ozeki, T. Nakayama, A. Ogata, K. Gotoh, K. Fujiwara, Electrochemical Na Insertion and Solid Electrolyte Interphase for Hard-Carbon Electrodes and Application to Na-Ion Batteries, Adv. Funct. Mater. 21 (2011) 3859–3867, https://doi.org/10.1002/adfm.201100854.
[49] X. Zhong, Y. Li, L. Zhang, J. Tang, X. Li, C. Liu, M. Shao, Z. Lu, H. Pan, B. Xu, High-Performance Sodium-Ion Batteries Based on Nitrogen-Doped Mesoporous Carbon Spheres with Ultrathin Nanosheets, ACS Appl. Mater. Interfaces 11 (2019) 2970–2977, https://doi.org/10.1021/acsami.8b17473.
[50] W.H. Bragg, W.L. Bragg, The reflection of X-rays by crystals, Proc. R. Soc. A 88 (1913) 428–438, https://doi.org/10.1098/rspa.1913.0040.
[51] S. Qiu, L. Xiao, M.L. Sushko, K.S. Han, Y. Shao, M. Yan, X. Liang, L. Mai, J. Feng, Y. Cao, X. Ai, H. Yang, J. Liu, Manipulating Adsorption–Insertion Mechanisms in Nanostructured Carbon Materials for High-Efficiency Sodium Ion Storage, Adv. Energy Mater. 7 (2017) 1700403, https://doi.org/10.1002/aenm.201700403.
[52] Y. Li, Y. Lu, Q. Meng, A.C.S. Jensen, Q. Zhang, Q. Zhang, Y. Tong, Y. Qi, L. Gu, M. Titirici, Y. Hu, Regulating Pore Structure of Hierarchical Porous Waste Cork-Derived Hard Carbon Anode for Enhanced Na Storage Performance, Adv. Energy Mater. 9 (2019) 1902852, https://doi.org/10.1002/aenm.201902852.
[53] Z. Zhu, W. Zhong, Y. Zhang, P. Dong, S. Sun, Y. Zhang, X. Li, Elucidating electrochemical intercalation mechanisms of biomass-derived hard carbon in sodium-/potassium-ion batteries, Carbon Energy 3 (2021) 541–553, https://doi.org/10.1002/cey2.111.
[54] M. Song, Q. Song, T. Zhang, X. Huo, Z. Lin, Z. Hu, L. Dong, T. Jin, C. Shen, K. Xie, Growing curly graphene layer boosts hard carbon with superior sodium-ion storage, Nano Res 16 (2023) 9299–9309, https://doi.org/10.1007/s12274-023-5539-8.
[55] Q. Li, J. Zhang, L. Zhong, F. Geng, Y. Tao, C. Geng, S. Li, B. Hu, Q.-H. Yang, Unraveling the Key Atomic Interactions in Determining the Varying Li/Na/K Storage Mechanism of Hard Carbon Anodes, Adv. Energy Mater. 12 (2022) 2201734, https://doi.org/10.1002/aenm.202201734.
[56] S. Qiu, L.F. Xiao, M.L. Sushko, K.S. Han, Y.Y. Shao, M.Y. Yan, X.M. Liang, L.Q. Mai, J.W. Feng, Y.L. Cao, X.P. Ai, H.X. Yang, J. Liu, Manipulating Adsorption-Insertion Mechanisms in Nanostructured Carbon Materials for High-Efficiency Sodium Ion Storage, Adv Energy Mater 7 (2017) 1700403, https://doi.org/10.1002/aenm.201700403. ARTN 1700403.
[57] G. Liu, Z. Wang, H. Yuan, C. Yan, R. Hao, F. Zhang, W. Luo, H. Wang, Y. Cao, S. Gu, C. Zeng, Y. Li, Z. Wang, N. Qin, G. Luo, Z. Lu, Deciphering Electrolyte Dominated Na^+ Storage Mechanisms in Hard Carbon Anodes for Sodium-Ion Batteries, Adv. Sci. 10 (2023) 2305414, https://doi.org/10.1002/advs.202305414.